J|A|C|S
JOURNAL OF THE AMERICAN CHEMICAL SOCIETY
pubs.acs.org/JACS
Article

Switching the Oxygen Evolution Mechanism on Atomically Dispersed Ru for Enhanced Acidic Reaction Kinetics

Yixin Hao, Sung-Fu Hung, Wen-Jing Zeng, Ye Wang, Chenchen Zhang, Chun-Han Kuo, Luqi Wang, Sheng Zhao, Ying Zhang, Han-Yi Chen, and Shengjie Peng*

Cite This: *J. Am. Chem. Soc.* 2023, 145, 23659−23669

Read Online

ACCESS | Metrics & More | Article Recommendations | Supporting Information

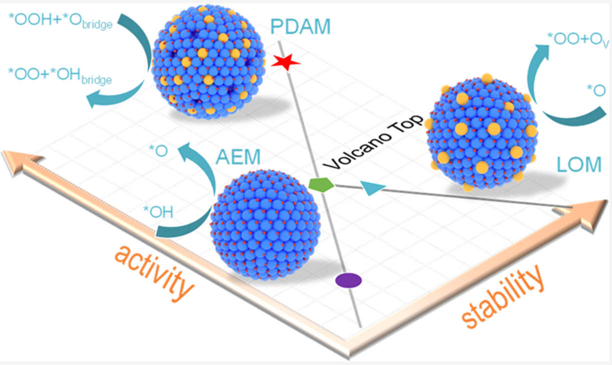

ABSTRACT: Designing stable single-atom electrocatalysts with lower energy barriers is urgent for the acidic oxygen evolution reaction. In particular, the atomic catalysts are highly dependent on the kinetically sluggish acid−base mechanism, limiting the reaction paths of intermediates. Herein, we successfully manipulate the steric localization of Ru single atoms at the Co_3O_4 surface to improve acidic oxygen evolution by precise control of the anchor sites. The delicate structure design can switch the reaction mechanism from the lattice oxygen mechanism (LOM) to the optimized adsorbate evolution mechanism (AEM). In particular, Ru atoms embedded into cation vacancies reveal an optimized mechanism that activates the proton donor−acceptor function (PDAM), demonstrating a new single-atom catalytic pathway to circumvent the classic scaling relationship. Steric interactions with intermediates at the anchored Ru−O−Co interface played a primary role in optimizing the intermediates' conformation and reducing the energy barrier. As a comparison, Ru atoms confined to the surface sites exhibit a lattice oxygen mechanism for the oxygen evolution process. As a result, the delicate atom control of the spatial position presents a 100-fold increase in mass activity from 36.96 A $g_{Ru(ads)}^{-1}$ to 4012.11 A $g_{Ru(anc)}^{-1}$ at 1.50 V. These findings offer new insights into the precise control of single-atom catalytic behavior.

■ INTRODUCTION

Acidic oxygen evolution reaction (OER) has long relied on precious Ir/Ru oxide catalysts, which have plagued the commercialization of the proton exchange membrane water electrolysis (PEMWE) technology. In this respect, the design of single-atom electrocatalysts is promising for maximizing atom utilization and optimizing the synergistic effect between active sites.[1−3] In most cases, the catalytic performance of single-atom catalysts (SACs) depends on the properties given in the properties of support materials since the electronic states can be regulated by the local coordination environment of anchoring.[4−7] Currently, oxide supports have been widely investigated to prevent undesirable agglomeration of active atoms.[8−10] These M−O−Ru (M: metal) moieties exhibit insufficient activity and stability due to the mismatch of the electronic structure and the thermodynamic instability of the active site. Typically, this drawback can be interpreted as target-anchored Ru single atoms with fewer electron cloud density and d electrons, leading to weakened OER reactivity.[11] The selection of electron-donating oxide substrates is an effective modulation strategy to inhibit the enhancement of the Ru oxidation state at the oxidation potential.[12−14] However, Ru SACs supported on the same substrate often exhibit deviations from the regular activity in the actual situation. In general, during the synthesis of SACs, noble metal single atoms often suffer from surface spillover or adsorption at surface oxygen defects due to atomic compatibility, resulting in mismatch between the electronic structure and theoretical activity,[15−17] which increases the design difficulty for SACs. In addition, it is still difficult to define whether the traditional Eley−Rideal-type adsorbate evolution mechanism and the two-dimensional interface concept are applicable to zero-dimensional SACs during the acidic OER process. Therefore, the precise control of anchor points is necessary to achieve real spatial homogeneity and to further analyze the catalytic behavior.

Based on the above considerations, steric interactions provide an effective strategy to design SACs that offer promising electrocatalytic activity. It is understood that the geometrical structural features of individual metal atoms on stable oxide supports contain both attachment to oxide

Received: July 21, 2023
Published: October 23, 2023

ACS Publications

https://doi.org/10.1021/jacs.3c07777

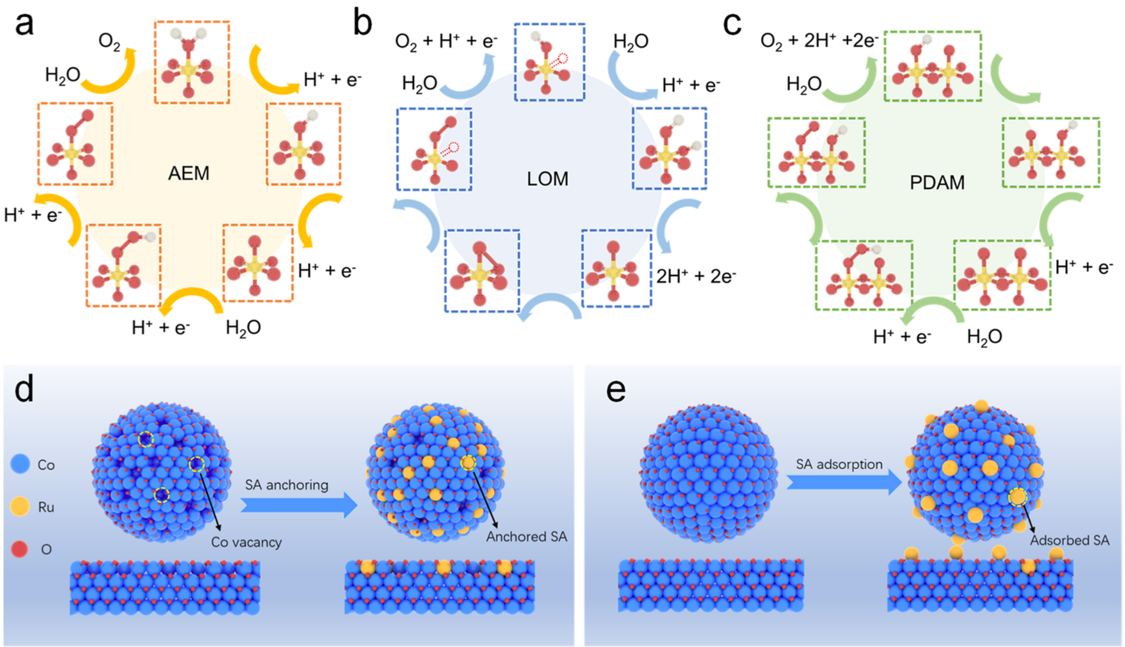

Figure 1. Illustration of the catalytic mechanisms of atomically dispersed ruthenium sites (a−c): simplified OER mechanisms consist of adsorbate evolution mechanism (AEM), lattice oxygen mechanism (LOM), and proton donor−acceptor mechanism (PDAM). (d, e) Schematic illustration of metal defective and perfect surface for anchoring Ru single atoms. Both catalysts exhibit single-atom level dispersion but completely different steric locations.

surfaces and embedding in the oxide lattice through strong covalent metal−support interactions. The dispersion and metal utilization efficiencies may be identical but are completely different in terms of isolation properties. These single-site centers change the local interfacial electronic structure to exhibit different catalytic pathways through site-resistance effects.[18−20] For instance, the single atom located at the hollow site and oxygen vacancy site exhibit different electronic affinities to oxygenated intermediates.[20] Hence, it is essential to correlate the space electronic state of the active metal species with the acidic catalytic behavior. To better explore the most favorable single-atom anchor point for the acidic OER reaction, constructing different steric configurations of lattice-anchored (Ru_{anc}) and surface-adsorbed (Ru_{ads}) ruthenium SACs is urgently needed. These atomically dispersed single sites are uniformly distributed in precisely defined steric locations. From a crystallographic point of view, Ru atoms in different active nanodomains can be coordinated to different numbers of oxygen species and exhibit diverse geometric configurations. Thus, steric interactions are expected to modulate the orbital occupancy of the Ru atoms and further influence the dissociation behavior of intermediates, thus modulating the OER activity.

In this work, steric homogeneity of atomic catalysis is achieved by synchronizing the metal defect construction with the single-atom anchoring. The atomic details and energies of intermediates at potentials relevant to oxygen evolution in acids are elucidated by comparing physical, steric, and electronic differences. In situ infrared absorption spectroscopy shows that Ru_{ads} exhibits an OER mechanism dominated by the lattice oxygen mechanism pathway, while Ru_{anc} is an adsorbate evolution mechanism that activates the proton donor−acceptor function, demonstrating a new pathway for SACs that circumvented the scaling relationship. Combining theoretical calculations and operando X-ray absorption spectroscopy (XAS), the desorption of mutually coupled distal and adsorbed *OO species is rate-determining, resulting in instability for Ru_{ads} species. On the contrary, the bridging oxygen sites can act as a proton acceptor to accelerate proton mobility for Ru_{anc}, leading to a break in the single adsorption−dissociation linear relationship, which in turn increases the OER activity. As a result, only an overpotential of 198.5 mV is required to drive the OER at 10 mA cm^{-2} for $Ru_{(anc)}-Co_3O_4$, which is significantly lower than the 298.1 mV of $Ru_{(ads)}-Co_3O_4$. Furthermore, the mass activity of $Ru_{(anc)}-Co_3O_4$ far exceeds most of the currently reported single-atom catalysts. The insight into the single-atom catalytic behavior at different steric coordinates provides a new perspective on the OER mechanism of SACs in acidic media and inspires us to design high-performance acidic OER catalysts.

RESULTS AND DISCUSSION

Mechanism Designs and Synthesis. As shown in Figure 1a,b, the oxygen evolution mechanism of single-site Ru mainly includes two types of AEM and LOM in acidic media. The LOM pathway involves direct coupling between intermediates and lattice oxygen, which has been proven to be more favorable for kinetics.[11] However, it is inevitably accompanied by the dissolution of RuO_4, which is disastrous and undesirable for single-atom catalysts. The conventional AEM mechanism exhibits a simultaneous transfer of electron−protons and therefore a linear relationship and large theoretical overpotential for the adsorption energy of O*, *OH, and *OOH. Assuming that the active center shifts from planar to 3D, this would facilitate proton transfer from the oxygen intermediate to the neighboring bridging oxygen site and allow independent binding energy optimization of the reaction intermediate (Figure 1c). Inspired by the above results, the steric location of the active site was designed by constructing metal defects, with

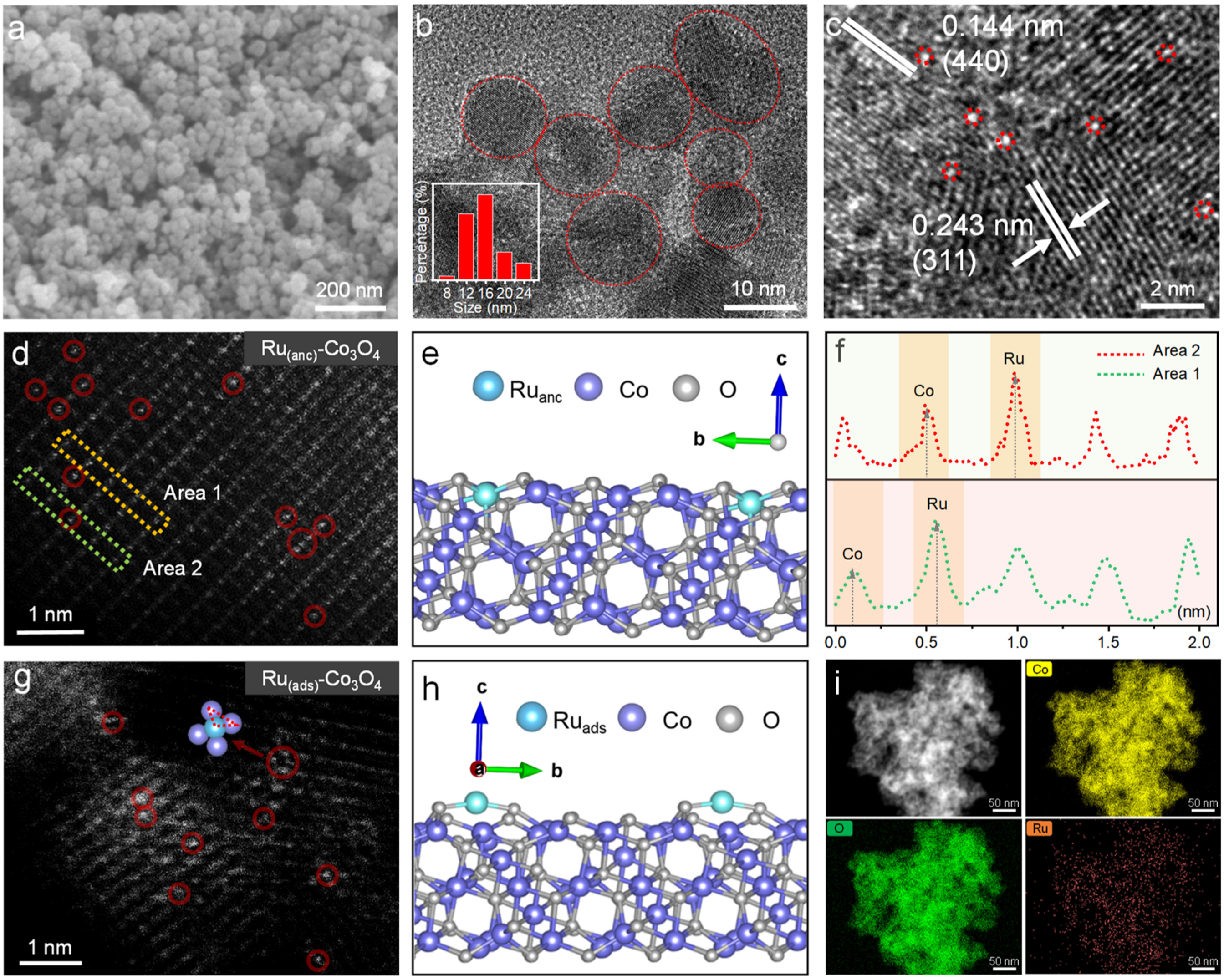

Figure 2. Characterization of metal defect-confined and surface-adsorbed atomic Ru in Co_3O_4. (a) Scanning electron microscopy (SEM), (b) TEM, and (c) high resolution-TEM (HR-TEM) images of $Ru_{(anc)}-Co_3O_4$. The inset in panel (b) is the corresponding nanoparticle size distribution, (d) HAADF-STEM, (e) simulated images of the anchored Ru single atom taken along the [111] orientation, and (f) the corresponding intensity profile of the parent Co_3O_4 along the dashed rectangles, showing the isolated arrangement of Ru atoms. (g, h) HAADF-STEM and simulated images of adsorbed atomic Ru. (i) TEM spectrum elemental mappings of $Ru_{(anc)}-Co_3O_4$ show the distribution of the Co, O, and Ru.

the aim of exploring the possibility of spatial interaction conversion reaction mechanism.

The anchored Ru with steric homogeneity is ingeniously achieved by synchronizing the construction of metal defects with the anchoring of single atoms. It is known that glycerolatocobalt (GlyCo) is a layered organometallic compound consisting of Co−O−Co−O skeletal parallel chains terminated by −O−C−C(C−OH)−O− groups.[21−23] During its thermal oxidation, the surface hydrocarbon groups are decomposed and removed, leaving an oxygen-rich environment and eventually the formation of inherent Co defects (Figures S1−S5). $Ru_{(anc)}-Co_3O_4$ was obtained by the diffusion of dissolved Ru ions into the interlayer anchorage of GlyCo where the cobalt defects formed in situ were utilized. For comparison, a series of $Ru_{(anc)}-Co_3O_4-X$ (X refers to the concentration of Ru elements) were also synthesized as described above. As a representative, $Ru_{(anc)}-Co_3O_4$ in the following refers to the best-performing catalyst $Ru_{(anc)}-Co_3O_4$-5 unless otherwise stated. $Ru_{(ads)}-Co_3O_4$ was formed by the electrostatic adsorption of cobalt oxides to surface Ru atoms (Figure 1d,e).

Morphological and Structural Characterization. $Ru_{(anc)}-Co_3O_4$ are composed of uniformly sized nanoparticles with an average diameter of around 16 nm (Figure 2a,b). By focusing on individual nanoparticles in Figure 2c, well-defined lattice fringes are assigned to the (311) and (440) planes of $Ru_{(anc)}-Co_3O_4$ lattices with spacings of 0.243 and 0.144 nm, respectively. The high-angle annular dark-field scanning transmission electron microscopy (HAADF-STEM) images of $Ru_{(anc)}-Co_3O_4$ nanocrystals observed along the crystal orientation of [111] exhibit ordered Co atomic arrays. Some of the brighter atomic columns are identified as Ru (Figure 2d,e), which is further confirmed by the intensity profile along the dotted box in Figure 2f. Moreover, the absence of aggregated ruthenium clusters indicates that the substitution of Ru atoms occurs mainly at the lattice sites and displays strong structural stability. In contrast, the STEM image of $Ru_{(ads)}-Co_3O_4$ shows a random distribution of Ru atoms in the middle of the Co

https://doi.org/10.1021/jacs.3c07777
J. Am. Chem. Soc. 2023, 145, 23659−23669

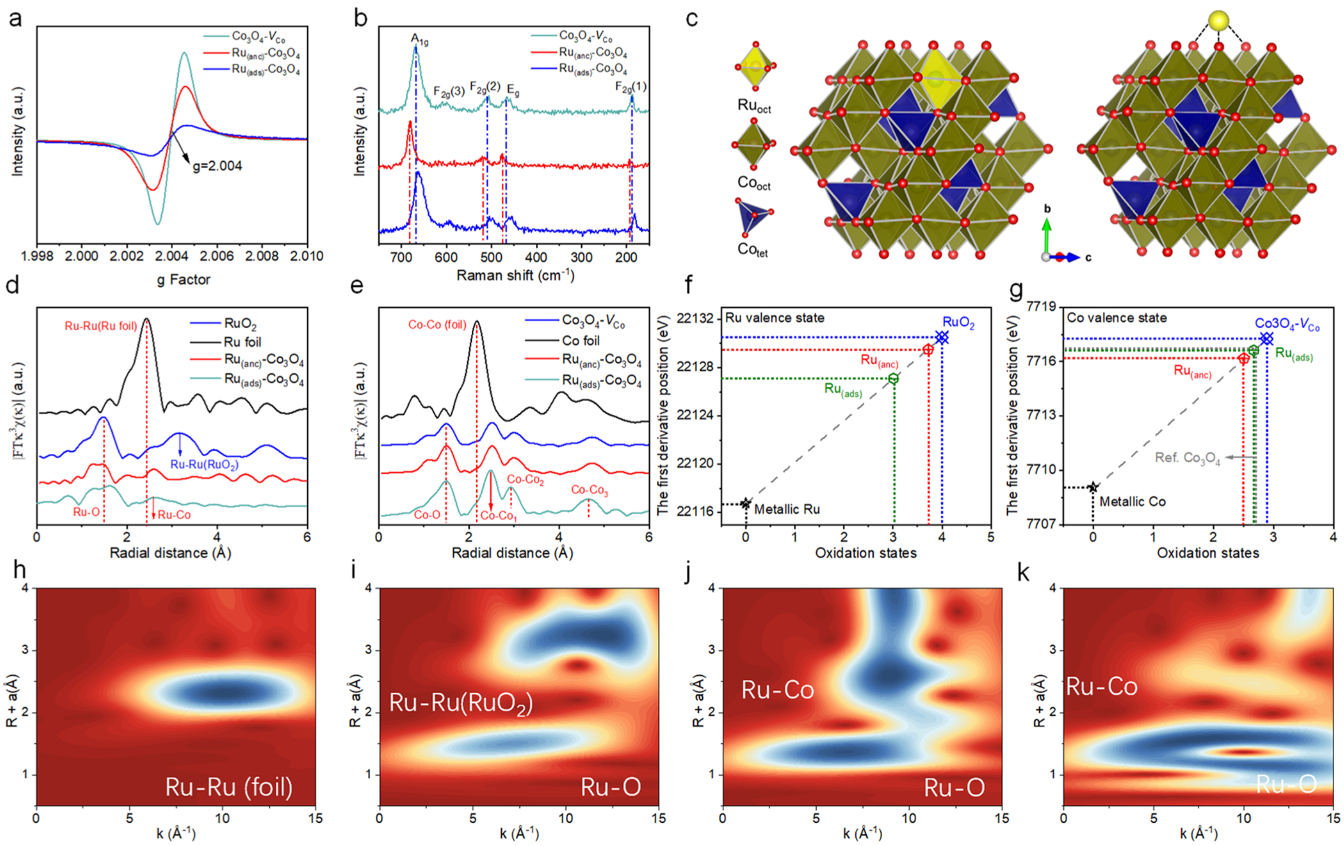

Figure 3. Structure properties of $Ru_{(anc)}$−Co_3O_4 and $Ru_{(ads)}$−Co_3O_4. (a) EPR and (b) Raman spectra. (c) Three-dimensional visualization of the topology illustration of $Ru_{(anc)}$−Co_3O_4 and $Ru_{(ads)}$−Co_3O_4. (d) Fourier transforms of the EXAFS spectra at Ru of Ru foil, RuO_2, $Ru_{(anc)}$−Co_3O_4, and $Ru_{(ads)}$−Co_3O_4. (e) Fourier-transform spectra from EXAFS at the Co K-edge of Co foil, Co_3O_4−V_{Co}, $Ru_{(anc)}$−Co_3O_4, and $Ru_{(ads)}$−Co_3O_4. Plot of the first derivative peak position K-edge energy vs oxidation state including (f) Ru and (g) Co collected from metal calibration foil. (h−k) WT-EXAFS of Ru foil RuO_2, $Ru_{(anc)}$−Co_3O_4 and $Ru_{(ads)}$−Co_3O_4 at the Ru K-edge, demonstrating highly dispersed single atoms in the catalysts.

nodes or at the edge of the grains (Figure 2g). In addition, the Ru atoms identified in the triangular lattice interstice correspond to the simulated image (Figure 2h). The above data suggest that Co defects in the −Co−O−Co− skeleton can trap individual Ru during high-temperature pyrolysis and promote the formation of lattice-confined Ru atoms. Importantly, single-atom Ru with differentiated steric positions possibly exhibits unique electronic structures and catalytic behavior.

Due to the ultralow loading capacity of Ru (around 3.23%, Table S1), the X-ray diffraction (XRD) patterns of $Ru_{(anc)}$−Co_3O_4 and $Ru_{(ads)}$−Co_3O_4 are imperceptibly shifted compared with the original Co_3O_4−V_{Co} (Figure S8). As shown by electron paramagnetic resonance (EPR) in Figure 3a, a visible signal is detected at 2.004, assigned to a Co vacancy.[22] And $Ru_{(anc)}$−Co_3O_4 has a weaker signal than Co_3O_4−V_{Co}, which further proves the success of the defect trapping technique to confine the Ru single atom to the lattice. The Raman bands within 150−750 cm^{-1} describe the intrinsic active modes of Co_3O_4 at about 189 cm^{-1} (F_{2g}), 466 cm^{-1} (E_g), 509 cm^{-1} (F_{2g}), 605 cm^{-1} (F_{2g}), and 668 cm^{-1} (A_{1g}).[24−26] The overall red shift of the $Ru_{(anc)}$−Co_3O_4 Raman bands compared to that of Co_3O_4−V_{Co} indicates a gradual increase in short-range ordering. In addition, this defective anchoring enhancement of short-range ordering is also manifested in the crystallinity enhancement caused by the change in the amount of anchoring (Figures S9 and S10). Notably, the A_{1g} band has a strong sensitivity to octahedral cationic vibrational changes and shows a more pronounced peak shift compared to the tetrahedral-dependent F_{2g} band, implying that the Ru atoms prefer to be anchored in octahedral positions rather than tetrahedral.[27] On the contrary, the insignificant offset of $Ru_{(ads)}$−Co_3O_4 indicates that the adsorption of Ru atoms on the surface does not cause lattice expansion. Therefore, the structural model was simulated based on the steric position where the Ru ion occupies the octahedral position, which is consistent with the structural analysis results.

The coordination environment of single-site Ru was further determined by using extended X-ray adsorption fine structure (EXAFS) spectroscopy. From Figure 3d, it can be seen that $Ru_{(anc)}$−Co_3O_4 and $Ru_{(ads)}$−Co_3O_4 deliver two significant peaks at 1.48 and 2.60 Å, respectively. The first shell contribution is caused by Ru−O scattering, and the scattering peak near 2.60 Å originates from the interaction of Ru−Co.[28,29] The Ru−Co bond distance is slightly longer than metallic Ru−Ru and shorter than RuO_2, which represents the single-atom character in the crystal structure and excludes the existence of Ru group clusters or particles. It is noteworthy that a significant coordination number difference of Ru-bound Co atoms in the second shell layer is observed, as reflected by the variation of the Ru−Co path intensity, which verifies that the ruthenium atoms of $Ru_{(anc)}$−Co_3O_4 are more present as Ru−Co pairs in a lattice-confined mode. Furthermore, there is only one significant Ru−O peak for $Ru_{(ads)}$−Co_3O_4 and the Ru−Co path is weak, suggesting that the single-site Ru is only riveted to exposed oxygen atoms. And the presence of longer Ru−O

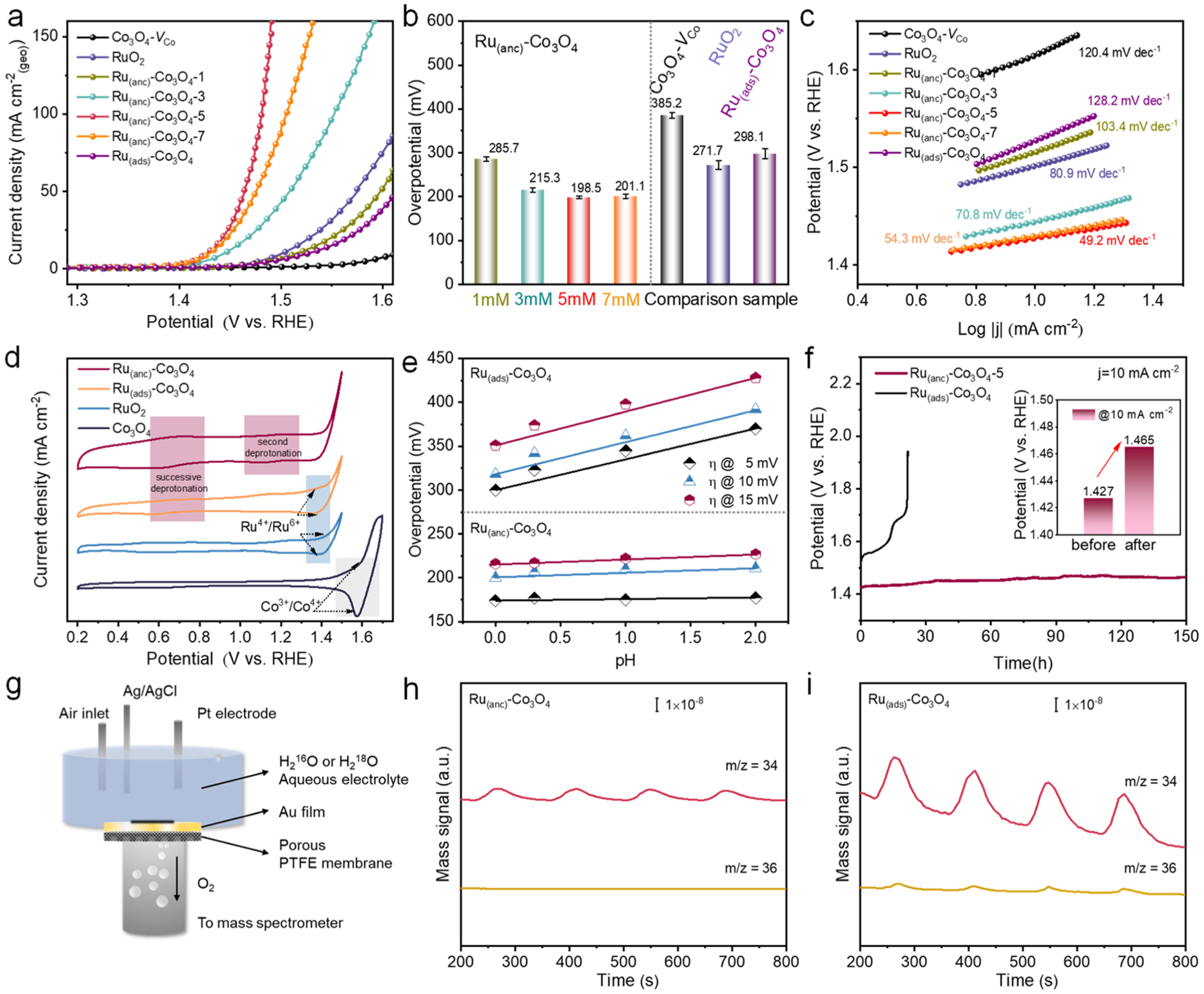

Figure 4. Oxygen evolution reaction activities in 0.5 M H_2SO_4 solution. (a) Oxygen evolution reaction polarization curves at a scan rate of 5 mV s^{-1} for RuO_2, Co_3O_4−V_{Co}, $Ru_{(ads)}$−Co_3O_4, and $Ru_{(anc)}$−Co_3O_4−X. (b) Overpotential histogram and (c) Tafel plots calculated from the iR-corrected polarization curves. (d) A comparison of the cyclic voltammogram curves without iR-corrected measured in argon-saturated 0.5 M H_2SO_4 at 50 mV s^{-1}. (e) pH dependence on the OER potential at different current densities for $Ru_{(anc)}$−Co_3O_4 and $Ru_{(ads)}$−Co_3O_4. (f) Chronopotentiometry test for $Ru_{(anc)}$−Co_3O_4 and $Ru_{(ads)}$−Co_3O_4 at 10 mA cm^{-2}. The inset shows the dissolved Ru mass percent in the H_2SO_4 of $Ru_{(anc)}$−Co_3O_4 after the 150 h test. (g) Schematic illustration of the operando DEMS (PTFE, polytetrafluoroethylene). DEMS measurements of $^{16}O^{18}O$ and $^{18}O^{18}O$ signals from the reaction products for ^{18}O-labeled (h) $Ru_{(anc)}$−Co_3O_4 and (i) $Ru_{(ads)}$−Co_3O_4 in 0.5 M H_2SO_4 in $H_2{}^{16}O$.

bonds is attributed to the surface coordination of unsaturated Ru−O octahedra. Normalized X-ray absorption near-edge structure (XANES) spectra at the Ru K-edge indicate that the valence states of $Ru_{(anc)}$−Co_3O_4 and $Ru_{(ads)}$−Co_3O_4 are between those of Ru foil and RuO_2 (Figure S14a,b). Using first derivative spectra to estimate the valence state (Figure 3f), the oxidation state of Ru in $Ru_{(anc)}$−Co_3O_4 is much similar to RuO_2, which can be attributed to the charge donation of coordinated cobalt species.[30,31] In contrast, the Ru valence of $Ru_{(ads)}$−Co_3O_4 is close to 3, implying a weaker electronic interaction between the surface-adsorbed ruthenium species and the cobalt tetraoxide. The valence states of the surface metal species were further examined to corroborate the consistent trend by X-ray photoelectron spectroscopy (XPS) as shown in Figure S12. The Ru coordination environment was further confirmed by wavelet transformation (Figure 3h−k). How the steric effect of Ru single atoms altered the electronic state of the Co_3O_4 support was further explored by XANES and EXAFS spectra of the Co k-edge. The valence state of $Ru_{(anc)}$−Co_3O_4 is significantly lower compared to that of the pristine Co_3O_4 with metal defects, which is caused by the charge transfer of cobalt stimulated by the lattice-closed Ru atoms. In contrast, the adsorbed Ru atoms of $Ru_{(ads)}$−Co_3O_4 produce negligible electronic modifications with a valence state similar to that of the baseline Co_3O_4. A closer look at the Co−O path and Co−Co1 path presented by the Cok-edge EXAFS spectra at 1.48 and 2.48 Å shows no significant bond length change before and after anchoring. This could be attributed to the broad anchoring degrees caused by the metal defect.

Oxygen Evolution Driven by Single-Site Ru. To establish the correlation between the catalytic activity and specific steric effects, OER performances are evaluated and compared to the benchmark. As shown by the polarization curves, commercial RuO_2 provides an overpotential of 271.7

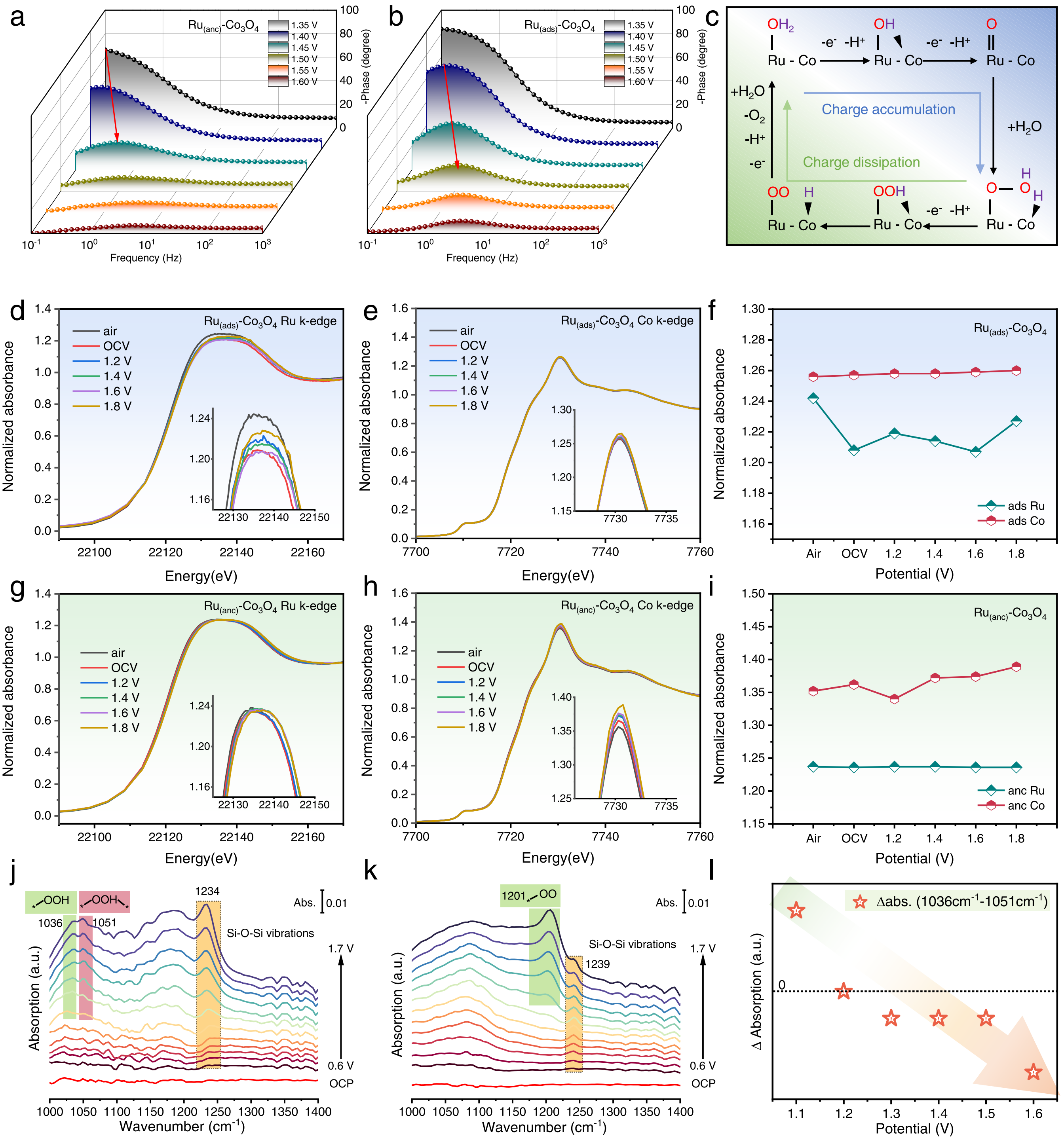

Figure 5. In situ EIS, ATR-SEIRAS, and XAFS spectra measurements. (a, b) The corresponding Bode plots of $Ru_{(anc)}-Co_3O_4$ and $Ru_{(ads)}-Co_3O_4$ measured at different potentials (phase angle relaxation as a function of frequency). (c) Proposed OER mechanism on the $Ru_{(anc)}-Co_3O_4$ under acidic conditions. (d, e) In situ XANES spectra of $Ru_{(ads)}-Co_3O_4$. (f) Changes in the normalized absorbance of Co and Ru in the in situ K-edge XANES spectra of $Ru_{(ads)}-Co_3O_4$. (g, h) In situ XANES spectra of $Ru_{(anc)}-Co_3O_4$. (i) Changes in the normalized absorbance of Co and Ru in the in situ K-edge XANES spectra of $Ru_{(anc)}-Co_3O_4$. (j, k) Operando attenuated total reflectance surface-enhanced infrared absorption spectroscopy (ATR-SEIRAS) measurements in the range of 1000−1400 cm^{-1} at various applied potentials, and all potentials were normalized against reversible hydrogen electrode. The vibrational band at wavenumber 1234 cm^{-1} is assigned to the Si−O−Si vibrations from the silicon substrate. (l) Intensity difference of the infrared signals at 1036 and 1051 cm^{-1} vs potentials for $Ru_{(anc)}-Co_3O_4$.

mV at 10 mA cm^{-2}, in agreement with previous reports.[32−34] It is evident that the anchoring quantity of the Ru atom directly affects the catalytic activity, where the preferred $Ru_{(anc)}-Co_3O_4$-5 displays not only a significant increase in activity compared to $Ru_{(ads)}-Co_3O_4$ but also an optimized performance to other single-atom OER catalysts reported so far (Figure 4a,b and Table S5). Specifically, $Ru_{(anc)}-Co_3O_4$-5 exhibited an overpotential as low as 198.5 mV at 10 mA cm^{-2} (Figure 4a,b), remarkably preceding $Ru_{(ads)}-Co_3O_4$ (298.1 mV). To quantify the intrinsic activity of the Ru atoms, the polarization current for the mass loading is normalized. $Ru_{(anc)}-Co_3O_4$-5 provides a high mass activity of 4012.11 A g^{-1} at a potential of 1.50 V, which is about 109 times higher than that of $Ru_{(ads)}-Co_3O_4$ (Figures S15−S17 and Tables S2 and S3). When the current density is normalized per ECSA, the specific activity of $Ru_{(anc)}-Co_3O_4$-5 still far exceeds that of $Ru_{(ads)}-Co_3O_4$. These results indicate that the steric location of the atom Ru is responsible for the high OER intrinsic activity. The Tafel slope provides more insight into the assessment of the OER reaction kinetics. As shown in Figure 4c, the slope (49.2 mV dec^{-1}) is much better than that of $Ru_{(ads)}-Co_3O_4$ (128.2 mV dec^{-1}) and commercial RuO_2 (80.9 mV dec^{-1}), also supporting the position-enhanced OER catalytic activity. The surface state trapping resistance (R1) and charge-transfer resistance (R2) of $Ru_{(anc)}-Co_3O_4$-5 measured by electrochemical impedance spectroscopy (EIS) are both at low levels, favoring the rapid proton−electron-transfer process at the catalyst−electrolyte interface, which is in agreement with the kinetic process verified by the Tafel eq (Figure S18 and Table S4).[35−37]

To investigate the proton transfer phenomenon of the catalysts, the electrochemical behavior during the redox transition was recorded. According to Figure 4d, the pre-OER redox features are observed in Co_3O_4, which are ascribed to equilibria of dimeric Co redox centers. In contrast, $Ru_{(ads)}-Co_3O_4$ and $Ru_{(anc)}-Co_3O_4$ have insignificant charge accumulation of the Co^{3+}/Co^{4+} redox couple, and this catalytic behavior change confirms that the activity is mainly related to the independent Ru. By focusing on the redox behavior near 1.4 V, it was found that the oxidation current of $Ru_{(ads)}-Co_3O_4$ increases slightly at 1.4 V (vs RHE) and the current does not increase sharply until 1.5 V, which corresponds to a redox transition of the surface proton-stabilized −OO(H) group similar to RuO_2 behavior. However, the cyclic voltammogram of $Ru_{(anc)}-Co_3O_4$ has insignificant characteristics before the onset of catalytic oxygen evolution, which demonstrates a fully oxidized surface and also implies a shift in the rate-determining step and catalytic mechanism.[38] The corresponding activity change was explored in the pH range of the electrolytes 0−2 to determine the catalytic mechanism. $Ru_{(anc)}-Co_3O_4$ shows an acidity-independent property on the pH scale, which is typical of the adsorbate evolution mechanism (Figure 4e).[30,39,40] In contrast, $Ru_{(ads)}-Co_3O_4$ reflects significant pH-dependent behavior associated with the unstable LOM mechanism. The activity difference implies the involvement of solution hydrogen protons and incompatibility of the proton−electron-transfer step with AEM. Correspondingly, the stability of $Ru_{(anc)}-Co_3O_4$ showed only a slight degradation during 150 h of continuous operation, while $Ru_{(ads)}-Co_3O_4$ underwent a substantial degradation after 12 h, which could be explained by the mechanism transformation.[34] In situ differential electrochemical mass spectroscopy (DEMS) measurements were further conducted using the isotope ^{18}O. $Ru_{(anc)}-Co_3O_4$ strictly follows the AEM, with no $^{36}O_2$ detected through DEMS (Figure 4h). A minimum amount of $^{34}O_2$ was detected in the OER products due to the natural isotopic abundance of ^{18}O in water. On the contrary, both $^{34}O_2$ and $^{36}O_2$ signals are detected during the OER for $Ru_{(ads)}-Co_3O_4$, which represent the engagement of lattice oxygen, thus confirming the initiation of the LOM (Figure 4i). Therefore, it is concluded that the acidic OER mechanism can be switched by the steric position, thus changing the reactivity of the structure.

In Situ Characterizations of the Structure and Intermediate Evolution. To reveal the charge and mass transfer processes of the Ru atoms, Operando EIS tests were performed at different applied biases as an effective method to follow dynamic interfacial evolution. Primarily, the applied bias during the OER reaction serves the reaction site indirectly but affects the polarization current in the form of charge accumulation.[41−43] As shown in the Bode plot (Figure 5a), with increasing bias, the pre-OER process for $Ru_{(anc)}-Co_3O_4$ induces a nonuniform distribution of surface charge manifested by a decrease in frequency peaks and a shift to higher frequencies over the range of 1.40−1.45 V. The charge accumulation is accompanied by a surface deprotonation coupling electron-transfer process, which in turn triggers a decrease in the activation free energy.[41] As a comparison, $Ru_{(ads)}-Co_3O_4$ has a wide transition phase peak interval (1.40−1.50 V), which indicates that the charge dissipation process is slow, and thus the efficiency of the oxidized charge shackles the OER surface reaction rate (Figure 5b). This pseudocapacitance behavior accompanying the Ru redox couple can be further matched onto the CV curve, specifically the pair of peaks of $Ru_{(ads)}-Co_3O_4$ near 1.4 V in Figure S21. The sluggish current growth slope can be found to coincide with a wide range of frequency peak shifts. In contrast, $Ru_{(anc)}-Co_3O_4$ has near-rectangular capacitive behavior and closely borders the sharply increasing polarization current region, implying that the surface deprotonation of the polarized OOH* is unsynchronized by an electron-transfer process. Therefore, for lattice-limited Ru atoms, additional chemical steps are possible such as the mentioned PDAM (Figure 5c).

To uncover the atomic details of the charge storage during the OER, in situ XAS spectra of $Ru_{(anc)}-Co_3O_4$ and $Ru_{(ads)}-Co_3O_4$ under different applied potentials (from 1.20 to 1.80 V vs RHE) were recorded. The intensity of white lines (IWL), measured as a function of applied potential, quantifies the number of empty orbit states and hence the oxidation state.[41] The IWL of $Ru_{(ads)}-Co_3O_4$ (Figure 5d,f) shows that the Ru oxidation state changes with bias, while the Co oxidation state remains constant. This finding implies that $Ru_{(ads)}-Co_3O_4$ is completely reliant on the valence change of the Ru center for the charge accumulation and dissipation and that the stepwise oxidation of Ru became the rate-limiting step in acidic conditions. On the contrary, the stable Ru oxidation state of $Ru_{(anc)}-Co_3O_4$ cannot fully account for the stored charge, implying that additional means are active, which is consistent with in situ EIS test results (Figure 5g). Furthermore, the Co IWL of $Ru_{(anc)}-Co_3O_4$ in the XANES exhibits a significant electron-transfer process during the OER compared to that of $Ru_{(ads)}-Co_3O_4$ (Figure 5h,i). These results indicate that the rate-determining step of the OER on $Ru_{(anc)}-Co_3O_4$ is not the valence change of Ru but the activation of the ligand, which implies the activation of PDAM.

In this study, Operando ATR-SEIRAS spectroscopy was used to identify reaction intermediates and to elucidate the influence of steric interactions on the reaction mechanism during oxygen evolution.[44] As the bias potential reaches the polarization region, a pair of distinct absorption peaks at 1036 and 1051 cm^{-1} were observed compared to the spectrum obtained under open-circuit potential conditions for $Ru_{(anc)}-Co_3O_4$, which indicates the production of oxygen intermediates (Figure 5j). The absorption peaks are identified as *OOH as an intermediate before the release of O_2 from AEM, and the

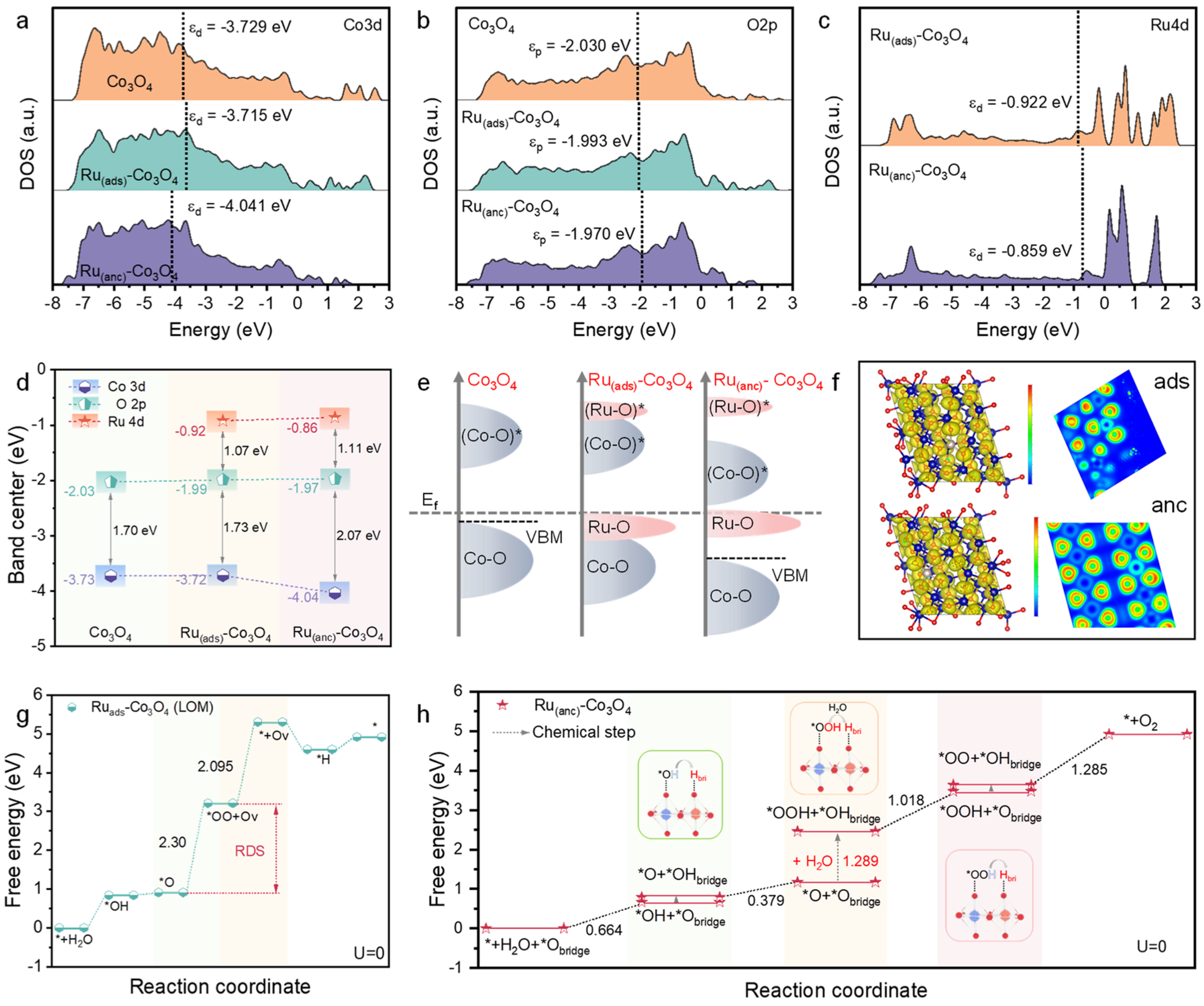

Figure 6. Proposed OER mechanism of lattice-confined and surface-adsorbed Ru single atoms on Co_3O_4. (a−c) Corresponding PDOS band centers of Co 3d orbital, Ru 4d orbital, and O 2p orbital in different models. (d) O p-band center of the p-band relative to Co and Ru. (e) Schematics relating this trend in models to the band center, which demonstrates the variation in VBM values and the formation of localized Ru−O hybridization states near E_f. (f) The top panels correspond to the charge density distribution on $Ru_{(anc)}−Co_3O_4$ and $Ru_{(ads)}−Co_3O_4$. (g) Gibbs free-energy diagram of $Ru_{(ads)}−Co_3O_4$ with LOM pathways. (h) Gibbs free-energy diagram of $Ru_{(anc)}−Co_3O_4$ with the PDAM mechanism for the activation of proton donor−acceptor function.

hump is attributed to the hydrogen bonds of *OOH with neighbors, which affects the molecular vibration.[45−47] To elucidate the dynamics of the deprotonation of the *OOH intermediate on the $Ru_{(anc)}$ surface, the difference in peak intensity of the absorption bands at 1036 and 1051 cm^{-1} was plotted as a function of applied bias in Figure 5l. Interestingly, the vibrational band intensity of hydrogen bonds between the *OOH intermediate and the Ru−O−Co surface increases significantly as the reaction potential increases. The phenomenon is attributed to the stronger interaction with H on surfaces that are fully oxidized at high potentials, implying an optimization of the proton adsorption energy at the bridging oxygen sites. The introduction of additional PDAM is in line with the inference of the in situ EIS, XAFS described above, which would accelerate the migration of protons at the Ru site, leading to a break in the single adsorption−dissociation linear relationship. For $Ru_{(ads)}−Co_3O_4$, a peak with a vibrational frequency of about 1200 cm^{-1} appears at a potential of 1.30 V (Figure 5k), which can be assigned to the stretching vibration of the *OO intermediate and the position of this absorption peak having been elucidated by the previously reported isotopic experiment.[45] This phenomenon is surprising in that the transfer of the Ru atom from the anchored position to a surface-adsorbed position caused a complete shift in the mechanism. Furthermore, a key piece of evidence is the absence of the *OOH intermediate symbolizing AEM detected near the 1050 cm^{-1} wavenumber on adsorbed single atomic surfaces.

Insights into the Oxygen Evolution Mechanism. Density functional theory calculations were further performed to clarify the mechanism transition caused by the steric effect, and the energetically favorable surface was chosen to simulate the OER process. In conjunction with experimental observations, the Ru atoms are anchored at the center of a six-coordinated cobalt octahedron in place of the Co position and are represented as a lattice-limited Ru single atom. Meanwhile,

https://doi.org/10.1021/jacs.3c07777
J. Am. Chem. Soc. 2023, 145, 23659−23669

the simulated surface-adsorbed Ru atoms are bonded to the three O of the adjacent Co−O polyhedra and protrude from the surface of Co_3O_4. Compared with the anchored Ru−O coordination, the adsorbed Ru single atom has a lower valence and significantly less coordinated O, which is consistent with the XAS results. Combined with the CV curves and in situ characterization observations, the initial polarization phase of the OER is not accompanied by a Co(III)/Co(IV) transition. That is, cobalt is absent from the quadruple electron-coupled proton transfer step and acts as an indirect reactivity center, so the acidic OER process preferentially proceeds at the Ru site. The following discussion is based on this premise. In either single-atom structure, the Ru introduces a new localized Ru 4d−O 2p-hybridized electronic state near the Fermi energy level, which endows the whole with more charge directly involved in the surface reaction and contributes to the reactivity (Figure 6c,f). In comparison, lattice-defined Ru has a d-band center closer to the Fermi energy level, further illustrating the role of spatial effects in regulating the evolution of reaction intermediates.

The degree of Ru−O−Co interaction affects the charge distribution and surface adsorption behavior. As shown in Figure 6d,e, the Co−O hybridization of $Ru_{(anc)}-Co_3O_4$ is relatively far from the Fermi energy level, which refers to the difficulty of losing valence electrons at the Co sites; namely, the lattice oxygen is challenging to be released by electrochemical oxidation. Therefore, the O−O coupling mechanism is thermodynamically unfavorable. In contrast, the Ru−O−Co bond of $Ru_{(ads)}-Co_3O_4$ has an overall high covalency, so direct O−O coupling is thermodynamically possible. To distinguish the effect of these different electronic structures on the catalytic performance, the energy details of the oxygen-released intermediates were evaluated according to the potential OER pathway.

For $Ru_{(ads)}-Co_3O_4$, a higher applied potential is required for further deprotonation, while the high covalency from Co−O−Ru promotes the activation of lattice oxygen and triggers the LOM mechanism that precedes the AEM process (Figure S23). As shown in Figure 6g, both the O−O coupling and release have high energy barriers but still outperform the traditional AEM pathway. Unlike the conventional RuO_2 oxide LOM mechanism, the coordination of the O atoms of adsorbed Ru and cobalt inhibits oxygen vacancy formation. The high vacancy formation energy leads to a still relatively difficult desorption of distal O from the lattice O and prevents producing a breakthrough enhancement. In addition, the generated oxygen vacancies lead to surface dissociation and rapid degradation of $Ru_{(ads)}-Co_3O_4$, as evidenced by the continuous decay of stability. Note that the *OOH intermediate for $Ru_{(anc)}-Co_3O_4$ is detected as early as 1.1 V vs RHE, which contradicts the rate-limiting step and confirms the inapplicability of the conventional AEM mechanism, so the analysis of additional chemical steps is necessary.[48,49] By integrating the above electrochemical features and in situ characterization, it is concluded that the lattice-defined Ru atom conformation with neighboring cobalt sites has an optimized geometry during the deprotonation. In this regard, adsorbed *OOH and *OH transfer the proton to the neighboring Co site. Compared with the adsorbed convex Ru−O−Co, the lattice-defined Ru−O−Co has a stronger steric interaction with *OOH and the bridging oxygen releases the proton into the cycle as the bias pressure increases. The detailed reaction pathway further revealed that the theoretical overpotential of the PDAM pathway for activating the proton donor−acceptor function is only 65 mV (Figure 6h). More importantly, the PDAM not only breaks the limitation of the reaction intermediate adsorption energy and activity interdependence but also maintains structural stability during the OER process. As a result, the simultaneous enhancement of stability and intrinsic activity was achieved.

CONCLUSIONS

In summary, we have manipulated the spatial localization of single-atom Ru by utilizing the metal defect anchor point of the support and switched the reaction mechanism. The atomic localization induces electronic change, and their spatially interacting distance effects have a direct impact on the adsorption conformation and dissociation steps of the intermediate, as directly confirmed by in situ ATR-SEIRAS and in situ XAFS characterization. The obtained $Ru_{(anc)}$-Co_3O_4 is capable of continuous operation for more than 150 h under acidic conditions without showing current decay and can reach an overpotential of 198 mV at 10 mA cm^{-2}. In addition to the Co_3O_4 lattice-defined Ru SACs, the proposed defect-anchored single-atom technique can also be applied to metal oxides derived from other transition-metal glycerol complexes, providing an effective and general way to construct a broad library of atomic-scale catalytic understanding.

ASSOCIATED CONTENT

Supporting Information

The Supporting Information is available free of charge at https://pubs.acs.org/doi/10.1021/jacs.3c07777.

Experimental details; additional experimental data and figures; and supporting discussion (PDF)

AUTHOR INFORMATION

Corresponding Author

Shengjie Peng − *College of Materials Science and Technology, Nanjing University of Aeronautics and Astronautics, Nanjing 210016, China*; orcid.org/0000-0003-1591-1301; Email: pengshengjie@nuaa.edu.cn

Authors

Yixin Hao − *College of Materials Science and Technology, Nanjing University of Aeronautics and Astronautics, Nanjing 210016, China*

Sung-Fu Hung − *Department of Applied Chemistry, National Yang Ming Chiao Tung University, Hsinchu 300, Taiwan*; orcid.org/0000-0002-7423-2723

Wen-Jing Zeng − *Department of Applied Chemistry, National Yang Ming Chiao Tung University, Hsinchu 300, Taiwan*

Ye Wang − *College of Materials Science and Technology, Nanjing University of Aeronautics and Astronautics, Nanjing 210016, China*

Chenchen Zhang − *Key Laboratory of Synthetic and Biological Colloids, Ministry of Education, School of Chemical and Material Engineering, Jiangnan University, Wuxi 214122 Jiangsu, China*

Chun-Han Kuo − *Department of Materials Science and Engineering, National Tsing Hua University, Hsinchu 30013, Taiwan*

Luqi Wang − *College of Materials Science and Technology, Nanjing University of Aeronautics and Astronautics, Nanjing 210016, China*

Sheng Zhao − *College of Materials Science and Technology, Nanjing University of Aeronautics and Astronautics, Nanjing 210016, China*

Ying Zhang − *Key Laboratory of Synthetic and Biological Colloids, Ministry of Education, School of Chemical and Material Engineering, Jiangnan University, Wuxi 214122 Jiangsu, China*

Han-Yi Chen − *Department of Materials Science and Engineering, National Tsing Hua University, Hsinchu 30013, Taiwan;* orcid.org/0000-0001-8146-7101

Complete contact information is available at: https://pubs.acs.org/10.1021/jacs.3c07777

Notes

The authors declare no competing financial interest.

ACKNOWLEDGMENTS

This work was supported by the National Natural Science Foundation of China (22075141 and 22101132), the Scientific and Technological Innovation Special Fund for Carbon Peak and Carbon Neutrality of Jiangsu Province (BK20220039), the Natural Science Foundation of Jiangsu Province (BK20221482 and BK20210311), the China Postdoctoral Science Foundation (2021M691561 and 2021T140319), the Jiangsu Postdoctoral Research Fund (2021K547C), the Fundamental Research Funds for the Central Universities (NS2023032), and the State Key Laboratory for Modification of Chemical Fibers and Polymer Materials, Donghua University (KF2312).

REFERENCES

(1) Yao, Y.; Hu, S.; Chen, W.; Huang, Z.-Q.; Wei, W.; Yao, T.; Liu, R.; Zang, K.; Wang, X.; Wu, G.; Yuan, W.; Yuan, T.; Zhu, B.; Liu, W.; Li, Z.; He, D.; Xue, Z.; Wang, Y.; Zheng, X.; Dong, J.; Chang, C.-R.; Chen, Y.; Hong, X.; Luo, J.; Wei, S.; Li, W.-X.; Strasser, P.; Wu, Y.; Li, Y. Engineering the electronic structure of single atom Ru sites via compressive strain boosts acidic water oxidation electrocatalysis. *Nat. Catal.* **2019**, *2* (4), 304−313.

(2) Kraushofer, F.; Parkinson, G. S. Single-atom catalysis: insights from model systems. *Chem. Rev.* **2022**, *122* (18), 14911−14939.

(3) Su, H.; Soldatov, M. A.; Roldugin, V.; Liu, Q. Platinum single-atom catalyst with self-adjustable valence state for large-current-density acidic water oxidation. *eScience* **2022**, *2* (1), 102−109.

(4) Gao, R.; Wang, J.; Huang, Z.-F.; Zhang, R.; Wang, W.; Pan, L.; Zhang, J.; Zhu, W.; Zhang, X.; Shi, C.; Lim, J.; Zou, J.-J. Pt/Fe_2O_3 with Pt−Fe pair sites as a catalyst for oxygen reduction with ultralow Pt loading. *Nat. Energy* **2021**, *6* (6), 614−623.

(5) Yu, D.; Ma, Y.; Hu, F.; Lin, C.-C.; Li, L.; Chen, H.-Y.; Han, X.; Peng, S. Dual-sites coordination engineering of single atom catalysts for flexible metal−air batteries. *Adv. Energy Mater.* **2021**, *11* (30), 2101242.

(6) Luo, F.; Hu, H.; Zhao, X.; Yang, Z.; Zhang, Q.; Xu, J.; Kaneko, T.; Yoshida, Y.; Zhu, C.; Cai, W. Robust and stable acidic overall water splitting on Ir single atoms. *Nano Lett.* **2020**, *20* (3), 2120−2128.

(7) Rao, P.; Wu, D.; Wang, T.-J.; Li, J.; Deng, P.; Chen, Q.; Shen, Y.; Chen, Y.; Tian, X. Single atomic cobalt electrocatalyst for efficient oxygen reduction reaction. *eScience* **2022**, *2* (4), 399−404.

(8) Ma, T.; Cao, H.; Li, S.; Cao, S.; Zhao, Z.; Wu, Z.; Yan, R.; Yang, C.; Wang, Y.; van Aken, P. A.; Qiu, L.; Wang, Y.-G.; Cheng, C. Crystalline lattice-confined atomic Pt in metal carbides to match electronic structures and hydrogen evolution behaviors of platinum. *Adv. Mater.* **2022**, *34* (41), 2206368.

(9) Yin, J.; Jin, J.; Lu, M.; Huang, B.; Zhang, H.; Peng, Y.; Xi, P.; Yan, C.-H. Iridium single atoms coupling with oxygen vacancies boosts oxygen evolution reaction in acid media. *J. Am. Chem. Soc.* **2020**, *142* (43), 18378−18386.

(10) Huang, H.; Yu, D.; Hu, F.; Huang, S.-C.; Song, J.; Chen, H.-Y.; Li, L. L.; Peng, S. Clusters induced electron redistribution to tune oxygen reduction activity of transition metal single-atom for metal−air batteries. *Angew. Chem., Int. Ed.* **2022**, *61* (12), e202116068.

(11) Chen, Z.; Guo, L.; Pan, L.; Yan, T.; He, Z.; Li, Y.; Shi, C.; Huang, Z.-F.; Zhang, X.; Zou, J.-J. Advances in oxygen evolution electrocatalysts for proton exchange membrane water electrolyzers. *Adv. Energy Mater.* **2022**, *12* (14), 2103670.

(12) Zhu, Y.; Wang, J.; Koketsu, T.; Kroschel, M.; Chen, J.-M.; Hsu, S.-Y.; Henkelman, G.; Hu, Z.; Strasser, P.; Ma, J. Iridium single atoms incorporated in Co_3O_4 efficiently catalyze the oxygen evolution in acidic conditions. *Nat. Commun.* **2022**, *13* (1), No. 7754.

(13) Liu, Y.; Chen, Y.; Mu, X.; Wu, Z.; Jin, X.; Li, J.; Xu, Y.; Yang, L.; Xi, X.; Jang, H.; Lei, Z.; Liu, Q.; Jiao, S.; Yan, P.; Li, X.; Cao, R. Spinel-anchored iridium single atoms enable efficient acidic water oxidation via intermediate stabilization effect. *ACS Catal.* **2023**, *13* (6), 3757−3767.

(14) Lee, J.; Kumar, A.; Kim, M. G.; Yang, T.; Shao, X.; Liu, X.; Liu, Y.; Hong, Y.; Jadhav, A. R.; Liang, M.; Tran, N. Q.; Lee, H. Single-metal-atom dopants increase the lewis acidity of metal oxides and promote nitrogen fixation. *ACS Energy Lett.* **2021**, *6* (12), 4299−4308.

(15) Wang, A.; Li, J.; Zhang, T. Heterogeneous single-atom catalysis. *Nat. Rev. Chem.* **2018**, *2* (6), 65−81.

(16) Zhu, J.; Cai, L.; Tu, Y.; Zhang, L.; Zhang, W. Emerging ruthenium single-atom catalysts for the electrocatalytic hydrogen evolution reaction. *J. Mater. Chem. A* **2022**, *10* (29), 15370−15389.

(17) Lang, R.; Du, X.; Huang, Y.; Jiang, X.; Zhang, Q.; Guo, Y.; Liu, K.; Qiao, B.; Wang, A.; Zhang, T. Single-atom catalysts based on the metal−oxide interaction. *Chem. Rev.* **2020**, *120* (21), 11986−12043.

(18) Feng, C.; Zhang, Z.; Wang, D.; Kong, Y.; Wei, J.; Wang, R.; Ma, P.; Li, H.; Geng, Z.; Zuo, M.; Bao, J.; Zhou, S.; Zeng, J. Tuning the electronic and steric Interaction at the atomic interface for enhanced oxygen evolution. *J. Am. Chem. Soc.* **2022**, *144* (21), 9271−9279.

(19) Wang, W.; Sharapa, D. I.; Chandresh, A.; Nefedov, A.; Heißler, S.; Heinke, L.; Studt, F.; Wang, Y.; Wöll, C. Interplay of electronic and steric effects to yield low-temperature CO oxidation at metal single sites in defect-engineered HKUST-1. *Angew. Chem., Int. Ed.* **2020**, *59* (26), 10514−10518.

(20) Zhang, Z.; Feng, C.; Wang, D.; Zhou, S.; Wang, R.; Hu, S.; Li, H.; Zuo, M.; Kong, Y.; Bao, J.; Zeng, J. Selectively anchoring single atoms on specific sites of supports for improved oxygen evolution. *Nat. Commun.* **2022**, *13* (1), No. 2473.

(21) Zhang, R.; Zhang, Y.-C.; Pan, L.; Shen, G.-Q.; Mahmood, N.; Ma, Y.-H.; Shi, Y.; Jia, W.; Wang, L.; Zhang, X.; Xu, W.; Zou, J.-J. Engineering cobalt defects in cobalt oxide for highly efficient electrocatalytic oxygen evolution. *ACS Catal.* **2018**, *8* (5), 3803−3811.

(22) Liu, X.; Zhao, L.; Xu, H.; Huang, Q.; Wang, Y.; Hou, C.; Hou, Y.; Wang, J.; Dang, F.; Zhang, J. Tunable cationic vacancies of cobalt oxides for efficient electrocatalysis in Li−O_2 batteries. *Adv. Energy Mater.* **2020**, *10* (40), 2001415.

(23) He, J.; Zou, Y.; Wang, S. Defective glycerolatocobalt(ii) for enhancing the oxygen evolution reaction. *Chem. Commun.* **2019**, *55* (85), 12861−12864.

(24) Nayak, S.; Dasari, K.; Joshi, D. C.; Pramanik, P.; Palai, R.; Sathe, V.; Chauhan, R. N.; Tiwari, N.; Thota, S. Spectroscopic studies of Co_2TiO_4 and $Co3O_4$ two-phase composites. *Phys. Status Solidi (b)* **2016**, *253* (11), 2270−2282.

(25) Zhang, R.; Pan, L.; Guo, B.; Huang, Z.-F.; Chen, Z.; Wang, L.; Zhang, X.; Guo, Z.; Xu, W.; Loh, K. P.; Zou, J.-J. Tracking the role of defect types in Co_3O_4 structural evolution and active motifs during oxygen evolution reaction. *J. Am. Chem. Soc.* **2023**, *145* (4), 2271−2281.

(26) Huang, J.; Sheng, H.; Ross, R. D.; Han, J.; Wang, X.; Song, B.; Jin, S. Modifying redox properties and local bonding of Co_3O_4 by

CeO_2 enhances oxygen evolution catalysis in acid. *Nat. Commun.* **2021**, *12* (1), No. 3036.

(27) Shan, J.; Ye, C.; Chen, S.; Sun, T.; Jiao, Y.; Liu, L.; Zhu, C.; Song, L.; Han, Y.; Jaroniec, M.; Zhu, Y.; Zheng, Y.; Qiao, S.-Z. Short-range ordered iridium single atoms integrated into cobalt oxide spinel structure for highly efficient electrocatalytic water oxidation. *J. Am. Chem. Soc.* **2021**, *143* (13), 5201−5211.

(28) Lian, Z.; Lu, Y.; Wang, C.; Zhu, X.; Ma, S.; Li, Z.; Liu, Q.; Zang, S. Single-atom Ru implanted on Co_3O_4 nanosheets as efficient dual-catalyst for Li-CO_2 batteries. *Adv. Sci.* **2021**, *8* (23), 2102550.

(29) Li, P.; Wang, M.; Duan, X.; Zheng, L.; Cheng, X.; Zhang, Y.; Kuang, Y.; Li, Y.; Ma, Q.; Feng, Z.; Liu, W.; Sun, X. Boosting oxygen evolution of single-atomic ruthenium through electronic coupling with cobalt-iron layered double hydroxides. *Nat. Commun.* **2019**, *10* (1), No. 1711.

(30) Shi, Z.; Wang, Y.; Li, J.; Wang, X.; Wang, Y.; Li, Y.; Xu, W.; Jiang, Z.; Liu, C.; Xing, W.; Ge, J. Confined Ir single sites with triggered lattice oxygen redox: toward boosted and sustained water oxidation catalysis. *Joule* **2021**, *5* (8), 2164−2176.

(31) Shen, R.; Chen, W.; Peng, Q.; Lu, S.; Zheng, L.; Cao, X.; Wang, Y.; Zhu, W.; Zhang, J.; Zhuang, Z.; Chen, C.; Wang, D.; Li, Y. High-concentration single atomic Pt sites on hollow CuS_x for selective O_2 reduction to H_2O_2 in acid solution. *Chem* **2019**, *5* (8), 2099−2110.

(32) Wang, X.; Wan, X.; Qin, X.; Chen, C.; Qian, X.; Guo, Y.; Xu, Q.; Cai, W.-B.; Yang, H.; Jiang, K. Electronic structure modulation of RuO_2 by TiO_2 enriched with oxygen vacancies to boost acidic O_2 evolution. *ACS Catal.* **2022**, *12* (15), 9437−9445.

(33) Wu, Z.-Y.; Chen, F.-Y.; Li, B.; Yu, S.-W.; Finfrock, Y. Z.; Meira, D. M.; Yan, Q.-Q.; Zhu, P.; Chen, M.-X.; Song, T.-W.; Yin, Z.; Liang, H.-W.; Zhang, S.; Wang, G.; Wang, H. Non-iridium-based electrocatalyst for durable acidic oxygen evolution reaction in proton exchange membrane water electrolysis. *Nat. Mater.* **2023**, *22* (1), 100−108.

(34) Wen, Y.; Chen, P.; Wang, L.; Li, S.; Wang, Z.; Abed, J.; Mao, X.; Min, Y.; Dinh, C. T.; Luna, P. D.; Huang, R.; Zhang, L.; Wang, L.; Wang, L.; Nielsen, R. J.; Li, H.; Zhuang, T.; Ke, C.; Voznyy, O.; Hu, Y.; Li, Y.; Goddard Iii, W. A.; Zhang, B.; Peng, H.; Sargent, E. H. Stabilizing highly active Ru sites by suppressing lattice oxygen participation in acidic water oxidation. *J. Am. Chem. Soc.* **2021**, *143* (17), 6482−6490.

(35) Qi, Y.; Zhang, Y.; Yang, L.; Zhao, Y.; Zhu, Y.; Jiang, H.; Li, C. Insights into the activity of nickel boride/nickel heterostructures for efficient methanol electrooxidation. *Nat. Commun.* **2022**, *13* (1), No. 4602.

(36) Liu, D.; Liu, J.-C.; Cai, W.; Ma, J.; Yang, H. B.; Xiao, H.; Li, J.; Xiong, Y.; Huang, Y.; Liu, B. Selective photoelectrochemical oxidation of glycerol to high value-added dihydroxyacetone. *Nat. Commun.* **2019**, *10* (1), No. 1779.

(37) Hao, Y.; Yu, D.; Zhu, S.; Kuo, C.-H.; Chang, Y.-M.; Wang, L.; Chen, H.-Y.; Shao, M.; Peng, S. Methanol upgrading coupled with hydrogen product at large current density promoted by strong interfacial interactions. *Energy Environ. Sci.* **2023**, *16* (3), 1100−1110.

(38) Rao, R. R.; Kolb, M. J.; Giordano, L.; Pedersen, A. F.; Katayama, Y.; Hwang, J.; Mehta, A.; You, H.; Lunger, J. R.; Zhou, H.; Halck, N. B.; Vegge, T.; Chorkendorff, I.; Stephens, I. E. L.; Shao-Horn, Y. Operando identification of site-dependent water oxidation activity on ruthenium dioxide single-crystal surfaces. *Nat. Catal.* **2020**, *3* (6), 516−525.

(39) An, L.; Wei, C.; Lu, M.; Liu, H.; Chen, Y.; Scherer, G. G.; Fisher, A. C.; Xi, P.; Xu, Z. J.; Yan, C.-H. Recent development of oxygen evolution electrocatalysts in acidic environment. *Adv. Mater.* **2021**, *33* (20), 2006328.

(40) Wang, K.; Wang, Y.; Yang, B.; Li, Z.; Qin, X.; Zhang, Q.; Lei, L.; Qiu, M.; Wu, G.; Hou, Y. Highly active ruthenium sites stabilized by modulating electron-feeding for sustainable acidic oxygen-evolution electrocatalysis. *Energy Environ. Sci.* **2022**, *15* (6), 2356−2365.

(41) Nong, H. N.; Falling, L. J.; Bergmann, A.; Klingenhof, M.; Tran, H. P.; Spöri, C.; Mom, R.; Timoshenko, J.; Zichittella, G.; Knop-Gericke, A.; Piccinin, S.; Pérez-Ramírez, J.; Cuenya, B. R.; Schlögl, R.; Strasser, P.; Teschner, D.; Jones, T. E. Key role of chemistry versus bias in electrocatalytic oxygen evolution. *Nature* **2020**, *587* (7834), 408−413.

(42) Ooka, H.; Yamaguchi, A.; Takashima, T.; Hashimoto, K.; Nakamura, R. Efficiency of oxygen evolution on iridium oxide determined from the pH dependence of charge accumulation. *J. Phys. Chem. C* **2017**, *121* (33), 17873−17881.

(43) Yang, S.; Li, X.; Li, Y.; Wang, Y.; Jin, X.; Qin, L.; Zhang, W.; Cao, R. Effect of proton transfer on electrocatalytic water oxidation by manganese phosphates. *Angew. Chem., Int. Ed.* **2023**, *62* (1), e202215594.

(44) Xue, Y.; Fang, J.; Wang, X.; Xu, Z.; Zhang, Y.; Lv, Q.; Liu, M.; Zhu, W.; Zhuang, Z. Sulfate-functionalized $RuFeO_x$ as highly efficient oxygen evolution reaction electrocatalyst in acid. *Adv. Funct. Mater.* **2021**, *31* (32), 2101405.

(45) Lin, Y.; Yu, L.; Tang, L.; Song, F.; Schlögl, R.; Heumann, S. In situ identification and time-resolved observation of the interfacial state and reactive intermediates on a cobalt oxide nanocatalyst for the oxygen evolution reaction. *ACS Catal.* **2022**, *12* (9), 5345−5355.

(46) Vivek, J. P.; Berry, N. G.; Zou, J.; Nichols, R. J.; Hardwick, L. J. In situ surface-enhanced infrared spectroscopy to identify oxygen reduction products in nonaqueous metal−oxygen batteries. *J. Phys. Chem. C* **2017**, *121* (36), 19657−19667.

(47) Lin, C.; Li, J.-L.; Li, X.; Yang, S.; Luo, W.; Zhang, Y.; Kim, S.-H.; Kim, D.-H.; Shinde, S. S.; Li, Y.-F.; Liu, Z.-P.; Jiang, Z.; Lee, J.-H. In-situ reconstructed Ru atom array on α-MnO_2 with enhanced performance for acidic water oxidation. *Nat. Catal.* **2021**, *4* (12), 1012−1023.

(48) Halck, N. B.; Petrykin, V.; Krtil, P.; Rossmeisl, J. Beyond the volcano limitations in electrocatalysis − oxygen evolution reaction. *Phys. Chem. Chem. Phys.* **2014**, *16* (27), 13682−13688.

(49) Wen, Y.; Liu, C.; Huang, R.; Zhang, H.; Li, X.; García de Arquer, F. P.; Liu, Z.; Li, Y.; Zhang, B. Introducing Brønsted acid sites to accelerate the bridging-oxygen-assisted deprotonation in acidic water oxidation. *Nat. Commun.* **2022**, *13* (1), No. 4871.